Dislocation dynamics in heterogeneous nanostructured materials

Shuozhi Xu [a,*], Justin Y. Cheng [b], Nathan A. Mara [b], Irene J. Beyerlein [a,c]

[a] *Department of Mechanical Engineering, University of California, Santa Barbara, CA 93106–5070, USA*
[b] *Department of Chemical Engineering and Materials Science, University of Minnesota, Minneapolis, MN 55455, USA*
[c] *Materials Department, University of California, Santa Barbara, CA 93106–5050, USA*

A B S T R A C T

Crystalline materials can be strengthened by introducing dissimilar phases that impede dislocation glide. At the same time, the changes in microstructure and chemistry usually make the materials less ductile. One way to circumvent the strength–ductility dilemma is to take advantage of heterogeneous nanophases which simultaneously serve as dislocation barriers and sources. Owing to their superior mechanical properties, heterogeneous nanostructured materials (HNMs) have attracted a lot of attention worldwide. Nevertheless, it has been difficult to characterize dislocation dynamics in HNMs using classical continuum models, mainly due to the challenges in describing the elastic and plastic heterogeneity among the phases. In this work, we advance a phase-field dislocation dynamics (PFDD) model to treat multi-phase materials, consisting of phases differing in composition, structural order, and size in the same system. We then apply the advanced PFDD model to exploring two important but divergent materials design problems in HNMs: dislocation/obstacle interactions and dislocation/interface interactions. Results show that the interactions between a dislocation and distribution of obstacles varying in structure and composition cannot be understood by simply interpolating from their individual interactions with a dislocation. It is also found that materials containing interfaces with nanoscale thicknesses and compositional gradients have a much higher dislocation bypass stress than those with sharp interfaces, providing an explanation for the simultaneous high strength and toughness of thick interface-containing nanolaminates as observed in recent experiments.

1. Introduction

Heterogeneous nanostructured materials (HNMs) are materials that are comprised of phases that vastly differ in their size, from micron to nanoscale, and in properties, such as elasticity and crystal structure. They are widespread in nature and actively used in many modern engineering applications as advanced smart and composite materials (Alexandrov and Zubarev, 2019). HNMs exhibit properties superior to either of their constituents combined as would be expected by rule-of-mixtures calculations (Wu et al., 2015; Wu and Zhu, 2017; Lu et al., 2020; Zhu et al., 2021). As an example, deformation in ductile crystalline materials is mainly controlled by dislocation slip, and so their strength and ductility can be attributed to the interactions of the nanophases with dislocations gliding in the micron matrix (Quek et al., 2014). Nanophase morphologies can range from gradient interfaces a few nanometers in thickness to an arrangement of both impenetrable and shearable precipitates (Zheng et al., 2013; Cheng et al., 2022).

Revealing the dynamics of dislocation interactions with heterogeneous phases aids in understanding the influence of nanostructures on mechanical behavior and how multi-obstacles and interfaces can be designed to achieve optimal material properties. In experiments, direct observation of discrete dislocations and their ability to overcome barriers, as well as direct measurement of

* Corresponding author.
  E-mail address: shuozhixu@ucsb.edu (S. Xu).

critical stresses and the barrier properties that control them, are challenging. Over the years, 3D computational models have been useful in identifying dislocation interaction mechanisms with different types of obstacles and interfaces (Beyerlein et al., 2019). The two main types of continuum mechanics approaches that have been developed specifically for dislocation motion in the presence of dissimilar phases are discrete dislocation dynamics (DDD) (Po et al., 2014; Bertin et al., 2020) and phase field dislocation models (Wang and Li, 2010). For predominantly crystalline HNMs, the phases can vary in number (two or more), morphology (nanoscale precipitate to gradient interfaces), structural order (amorphous vs. crystalline), and composition (void vs. alloy). The challenge that most continuum-based dislocation models have overcome to date is treating the elastic mismatch between two phases. Both DDD and phase field dislocation models have accomplished this by adopting a method introduced first by Eshelby (1957), who proposed that the disturbance of an inhomogeneity inside an elastic solid is equivalent to applying an uniform stress to the solid at a large distance. Wu et al. (2022), for instance, used DDD to predict the increase in the dislocation glide resistance caused by vacancy clusters. In that case the system contained two phases. Wang et al. (2003) developed a phase field microelasticity model for a system that contained three phases: substrate, thin film, and vacuum. The dislocation only glided in the first two phases. Zeng et al. (2016) developed a bi-phase phase-field dislocation dynamics (PFDD) model that was elastically and plastically heterogeneous. The dislocation could glide in two dissimilar phases, enabling a study of the effect of elastic and lattice mismatch on dislocation glide transfer across a bi-phase interface. Later, phase field models were presented in which the elastic anisotropy and defect energetics of both phases were captured (Mianroodi et al., 2019). More recently, Xu et al. (2022) extended the bi-phase PFDD model to include elastic anisotropy and dislocation dissociation. The model was applied to Cu/Nb nanolaminates with 3D interfaces to study the transmission of small dislocation pile-ups, as found in experiments (Cheng et al., 2022). Such extensions permit account of both long-range and short-range interactions when dislocations shear through crystalline phases or voids.

To model dislocation dynamics in general HNMs, where microstructural designs aim to exploit multiple dissimilar phases of varying substantially in properties, it is necessary to extend the bi-phase PFDD model to treat multi-phase materials where elastic anisotropy, dislocation core structure, and fault energies associated with dislocation glide in all phases, as appropriate, are taken into account. That is the main goal of this paper. Because dynamics can be simulated over longer periods of time, PFDD can assess multiple configurations of obstacles and interfaces, many different compositions and crystallographies of such obstacles, as well as multiple dislocations (Cheng et al., 2022), via controlling independently the individual role of elasticity and defect energetics. PFDD also provides stress states and strain rates closer to those in strained crystals than possible with atomistic methods. Another benefit of using phase-field dislocation model is that *ab initio* data can be used directly, compared with atomistic simulations which require high-quality interatomic potentials.

The remainder of this paper is organized as follows. In the Methods section, the PFDD formulation for multi-phase materials is presented in detail, followed by that model set-up and material parameters used in subsequent simulations are presented. Then in the Results and Discussion section, the new formulation is applied to dislocation dynamics in two important but distinct microstructures. Since dislocations themselves have different properties in face-centered cubic (FCC) and body-centered cubic (BCC) crystals, we choose either FCC Cu or BCC Nb as the model material as the predominant phase. The first problem involves the interactions between a dislocation and a set of nanoscale heterogeneous obstacles. The obstacles consist of arrays of nanophases with vastly distinct properties, such as voids, shearable crystalline precipitates, and unshearable amorphous precipitates. These obstacles are typical in HNMs (Peng et al., 2020; Noell et al., 2020). We report the critical stresses for a dislocation to bypass the obstacle arrays and the corresponding bypass mechanisms. The second problem considers slip transfer of a dislocation across a 3D interface in a Cu matrix. 3D interfaces are heterophase interfaces with nanoscale thickness and contain the chemical elements of the two adjacent crystals, from which the interfaces can be chemically and/or structurally distinct (Chen et al., 2020). In the current work, the interface is either homogeneous or heterogeneous, containing crystalline phases that are shearable by dislocations. Lastly, in the Conclusions section, implications of introducing multi-phase obstacles and interfaces and potential applications of the multi-phase PFDD model to other HNMs are discussed.

2. Methods

2.1. Multi-phase PFDD model

In this section, we present the PFDD formulation for an elastically heterogeneous medium that contains N_{mat} materials. We assume that the medium deforms elastically and, if it is a crystal, it may also deform plastically, where plasticity is accommodated by the glide of dislocations on preferred slip systems. Let ϕ be the order parameter set. Each order parameter ϕ_α is for each slip system α. The values $\phi_\alpha = 0$ and 1 represent the unslipped and slipped states, respectively. In the current work, ϕ_α is confined to be non-zero only in the slip plane of α (Xu et al., 2020a). Dislocations are assumed to always exist in material 1, but not necessarily in other materials. In what follows, let n_{op}, n_{sp}, and N_{sp} be the total number of order parameters, the number of order parameters per slip plane, and the total number of slip planes, respectively, in each material. These three numbers are related by $n_{\text{op}} = N_{\text{sp}} n_{\text{sp}}$.

The total energy density ψ consists of four terms: elastic energy density ψ_{ela}, lattice energy density ψ_{lat}, gradient energy density ψ_{gra}, and external energy density ψ_{ext}, i.e., at each continuum point x,

$$\psi(x) = \psi_{\text{ela}}(x) + \psi_{\text{lat}}(x) + \psi_{\text{gra}}(x) - \psi_{\text{ext}}(x). \tag{1}$$

The first energy density is the elastic energy density, ψ_{ela}, which represents the energy stored in the material surrounding the dislocation core. To formulate ψ_{ela}, we first define the eigenstrain (i.e., inelastic strain) tensor, ϵ^0, as

$$\epsilon^0(\boldsymbol{x}) = \begin{cases} \epsilon^{\text{p}}(\boldsymbol{x}), & \boldsymbol{x} \in \text{material } 1 \\ \epsilon^{\text{p}}(\boldsymbol{x}) + \epsilon^{\text{v}}(\boldsymbol{x}), & \boldsymbol{x} \in \text{material } N \text{ where dislocations exist } (N \neq 1) \\ \epsilon^{\text{v}}(\boldsymbol{x}), & \boldsymbol{x} \in \text{material } N \text{ where dislocations don't exist } (N \neq 1) \end{cases} \tag{2}$$

where ϵ^{p} and ϵ^{v} are the plastic strain tensor and virtual strain tensor, respectively. Among the two strain tensors, the first one is related to the plastic distortion tensor $\boldsymbol{\beta}^{\text{p}}$, and then to the order parameter $\boldsymbol{\phi}$, i.e.,

$$\epsilon^{\text{p}} = \text{sym}\,\boldsymbol{\beta}^{\text{p}} \tag{3}$$

$$\boldsymbol{\beta}^{\text{p}}(\boldsymbol{\phi}) = \sum_{\alpha=1}^{n_{\text{op}}} \frac{b_\alpha \phi_\alpha}{d_\alpha} \boldsymbol{s}_\alpha \otimes \boldsymbol{n}_\alpha \tag{4}$$

where $\boldsymbol{s}_\alpha$ is the slip direction unit vector, b_α is the slip vector magnitude, $\boldsymbol{n}_\alpha$ is the slip plane unit normal, and d_α is the interplanar spacing between two adjacent slip planes, for slip system α. Note that ϵ^{v} is independent of $\boldsymbol{\phi}$.

Then $\psi_{\text{ela}}(\boldsymbol{x})$ can be written as the sum of the "equivalent" homogeneous elastic energy density, $\psi_{\text{ela}}^{\text{eq}}(\boldsymbol{x})$, and the "extra" elastic energy density, $\psi_{\text{ela}}^{\text{ex}}(\boldsymbol{x})$, i.e. (Xu et al., 2022),

$$\psi_{\text{ela}}(\boldsymbol{x}) = \psi_{\text{ela}}^{\text{eq}}(\boldsymbol{x}) + \psi_{\text{ela}}^{\text{ex}}(\boldsymbol{x}) \tag{5}$$

where

$$\psi_{\text{ela}}^{\text{eq}}(\boldsymbol{x}) = \frac{1}{2}[\epsilon(\boldsymbol{x}) - \epsilon^0(\boldsymbol{x})] \cdot \boldsymbol{C}[\epsilon(\boldsymbol{x}) - \epsilon^0(\boldsymbol{x})] \tag{6}$$

$$\psi_{\text{ela}}^{\text{ex}}(\boldsymbol{x}) = \frac{1}{2}\epsilon^{\text{v}}(\boldsymbol{x}) \cdot \boldsymbol{M}^{[N]}(\boldsymbol{x})\epsilon^{\text{v}}(\boldsymbol{x}) \tag{7}$$

where $\boldsymbol{C}$ is the elasticity tensor and the strain tensor $\epsilon = \text{sym}\,\boldsymbol{\beta}$, where $\boldsymbol{\beta} = \nabla\boldsymbol{u}$ is the distortion with $\boldsymbol{u}$ being the displacement. In Eq. (7), $1 < N \leq N_{\text{mat}}$ and

$$M_{ijkl}^{[N]}(\boldsymbol{x}) = -C_{ijmn}^{[1]}\left[\Delta C_{mnpq}^{[N]}(\boldsymbol{x})\right]^{-1} C_{pqkl}^{[1]} - C_{ijkl}^{[1]} \tag{8}$$

where

$$\Delta C_{ijkl}^{[N]}(\boldsymbol{x}) = C_{ijkl}^{[N]}(\boldsymbol{x}) - C_{ijkl}^{[1]} \tag{9}$$

According to Eq. (2), the virtual strain tensor ϵ^{v} does not exist in material 1. Hence, $\psi_{\text{ela}}^{\text{ex}}$ exists in all materials but material 1.

The second energy density in Eq. (1), the lattice energy density, ψ_{lat}, represents the energy stored (i) within the intrinsic stacking fault (ISF) of a dissociated dislocation or (ii) within the core of an undissociated dislocation. ψ_{lat} is expressed as

$$\psi_{\text{lat}}(\boldsymbol{x}) = \frac{\gamma_{\text{gsf}}^{[N]}(\boldsymbol{\phi}(\boldsymbol{x}))}{l_{\text{gsf}}^{[N]}(\boldsymbol{x})} \tag{10}$$

where $\gamma_{\text{gsf}}^{[N]}$ is the GSFE as a function of the local order parameter $\boldsymbol{\phi}$ and $l_{\text{gsf}}^{[N]}$ is the spacing between the two adjacent slip planes based on which $\gamma_{\text{gsf}}^{[N]}$ is calculated. Both quantities are in material N, where $1 \leq N \leq N_{\text{mat}}$. In each material, when $n_{\text{sp}} = 1$, γ_{gsf} is represented by a GSFE curve; when $n_{\text{sp}} > 1$, γ_{gsf} is represented by a GSFE surface. The value of n_{sp} is pre-set, depending on prior knowledge of material N.

The third energy density in Eq. (1), the gradient energy density, ψ_{gra}, represents the energy stored within the two Shockley partial dislocation cores of a dissociated dislocation. With this physical meaning in mind, ψ_{gra} is written as a function of the order parameter gradient, i.e. (Wang et al., 2001; Xu et al., 2019b),

$$\psi_{\text{gra}}(\boldsymbol{x}) = \sum_{\alpha,\beta=1}^{n_{\text{sp}}^{[N]}} \eta_{\alpha\beta}^{[N]} \nabla\phi_\alpha(\boldsymbol{x}) \cdot \boldsymbol{\Xi}_{\alpha\beta}(\boldsymbol{x})\nabla\phi_\beta(\boldsymbol{x}) \tag{11}$$

where $\eta_{\alpha\beta}^{[N]}$ is the gradient energy coefficient for the order parameter sets $\alpha\beta$ in material N, where $1 \leq N \leq N_{\text{mat}}$, and

$$\boldsymbol{\Xi}_{\alpha\beta} = \frac{\boldsymbol{b}_\alpha \cdot \boldsymbol{b}_\beta}{d_\alpha d_\beta}[(\boldsymbol{n}_\alpha \cdot \boldsymbol{n}_\beta)\boldsymbol{I} - \boldsymbol{n}_\beta \otimes \boldsymbol{n}_\alpha] \tag{12}$$

where $\boldsymbol{I}$ is the identity tensor. Note that ψ_{lat} and ψ_{gra} only exist in materials that contain dislocations.

The last energy density in Eq. (1), the external energy density, ψ_{ext}, represents the energy arising from externally applied stress and/or strain. ψ_{ext} is expressed as

$$\psi_{\text{ext}}(\boldsymbol{x}) = \boldsymbol{\sigma}_{\text{app}} \cdot \epsilon^0(\boldsymbol{x}) \tag{13}$$

where $\boldsymbol{\sigma}_{\text{app}}$ is the applied stress tensor.

Table 1

Lattice parameters a_0 (in Å), elastic constants C_{11}, C_{12}, C_{44} (in GPa), and uniform gradient energy coefficients η (in μb^2) of the two pure metals and four random binary alloys studied in this work. a_0 of Cu and Nb are taken from *ab initio* calculations (Su et al., 2019a; Xu et al., 2020b). Elastic constants of Cu and Nb are taken from experiments (Warlimont and Martienssen, 2018). All data (except η) of the alloys are from recent atomistic simulations (Xu et al., 2022). Isotropic shear modulus in Voigt form $\mu = (3C_{44} + C_{11} - C_{12})/5$. The three non-zero η values are newly calculated in this work.

	Phase	a_0	C_{11}	C_{12}	C_{44}	μ	η
Cu	FCC	3.634	169	122	75.3	54.58	0.38
$Cu_{0.9}Nb_{0.1}$	FCC	3.699	187.25	135.8	81.88	59.42	0.28
$Cu_{0.8}Nb_{0.2}$	FCC	3.759	195.16	128.44	79.32	60.94	0.19
$Cu_{0.5}Nb_{0.5}$	Amorphous		193.7	135.9	30.8	30.04	0
$Cu_{0.1}Nb_{0.9}$	BCC	3.274	221.58	141.63	40.63	40.37	0
Nb	BCC	3.324	245	132	28.4	39.64	0

Once the energy functional is set and the order parameters are initialized, we minimize the total system energy with respect to each order parameter ϕ_α and each virtual strain component ϵ_{ab} (where $a, b = 1, 2, 3$) via the time-dependent Ginzburg–Landau equations, i.e.,

$$\dot{\phi}_\alpha(\boldsymbol{x}) = -m_0[\partial_{\phi_\alpha(\boldsymbol{x})}(\psi_{\text{ela}}(\boldsymbol{x}) + \psi_{\text{gsf}}(\boldsymbol{x}) - \psi_{\text{ext}}(\boldsymbol{x})) - \nabla \cdot \partial_{\nabla\phi_\alpha(\boldsymbol{x})}\psi_{\text{gra}}(\boldsymbol{x})] \tag{14}$$

$$\dot{\epsilon}_{ab}^{\text{v}}(\boldsymbol{x}) = -m_0^{\text{v}}\partial_{\epsilon_{ab}^{\text{v}}(\boldsymbol{x})}(\psi_{\text{ela}}(\boldsymbol{x}) - \psi_{\text{ext}}(\boldsymbol{x})) \tag{15}$$

where the superposed dot denotes the time derivative. The Ginzburg–Landau coefficients m_0 and m_0^{v}, in units of m·s/kg, are not necessarily the same but should both be non-negative. Note that Eq. (14) is applied to all materials while Eq. (15) is applied to all materials except material 1.

2.2. Model and material parameters

Matrices and crystalline precipitates in this work are either FCC or BCC phases. A single slip plane is considered, i.e., $N_{\text{sp}} = 1$, and so $n_{\text{sp}} = n_{\text{op}}$. Let a_0 be the lattice parameter. In FCC phases, the slip plane is {111} and the inter-planar spacing $l_{\text{gsf}} = d_\alpha = a_0/\sqrt{3}$. Within the plane, there are three slip vectors (i.e., $n_{\text{sp}} = 3$), each of which lies along a $\langle 110 \rangle$ direction with $b_\alpha = \sqrt{2}a_0/2$. Since $n_{\text{sp}} > 1$, γ_{gsf} is a GSFE surface. In BCC phases, the slip plane is {110}, in which there is only one slip vector along a $\langle 111 \rangle$ direction with $b_\alpha = \sqrt{3}a_0/2$. The inter-planar spacing $l_{\text{gsf}} = d_\alpha = a_0/\sqrt{2}$. Since $n_{\text{sp}} = 1$, γ_{gsf} is presented by a GSFE curve.

The crystallographic orientations of the simulation box and the grid spacings depend on the lattice type of the matrix. In an FCC matrix, the orientation is ($[\bar{1}10], [111], [11\bar{2}]$) and the grid spacings are ($\sqrt{2}a_0/4, \sqrt{3}a_0/3, \sqrt{6}a_0/4$). In a BCC matrix, they are ($[111], [\bar{1}10], [\bar{1}\bar{1}2]$) and ($\sqrt{3}a_0/2, \sqrt{2}a_0/2, \sqrt{6}a_0/3$), respectively.

The elastic energy density ψ_{ela} is calculated by the fast Fourier transform method. All Ginzburg–Landau coefficients are set to unity and the timestep size $\Delta t = 0.02$. Once the dislocations and obstacles or interfaces are initialized, a series of resolved shear stresses are independently applied to the system to drive the two edge dislocations to move apart. For each shear stress, iterations are terminated when the Euclidean norm of the difference in global vector of each order parameter and each virtual strain between successive iterations is smaller than 10^{-5}. The minimum applied stress subject to which each dislocation bypasses its closest obstacle array or interface is σ_0, and the critical stress $\sigma_{\text{c}} = \sigma_0 - 5 \times 10^{-5}\mu$, where μ depends on the matrix, as summarized in Table 1.

In this work, two types of matrices are considered; both are pure metals: Cu and Nb. Four random binary alloys are considered: $Cu_{0.1}Nb_{0.9}$, $Cu_{0.5}Nb_{0.5}$, $Cu_{0.8}Nb_{0.2}$, and $Cu_{0.9}Nb_{0.1}$. As found in our recent atomistic simulations (Xu et al., 2022), all six materials but $Cu_{0.5}Nb_{0.5}$ are crystals. All four random binaries are used to construct obstacles. Three crystalline random binaries are used to construct interfaces. For each crystalline material, PFDD requires the following: lattice parameter a_0, three independent elastic constants C_{11}, C_{12}, C_{44}, GSFE surface/curve γ_{gsf}, and gradient energy coefficients $\eta_{\alpha\beta}$. For the amorphous material, i.e., $Cu_{0.5}Nb_{0.5}$, only three elastic constants are needed for PFDD. Values of a_0, C_{11}, C_{12}, C_{44}, and γ_{gsf} in all materials are from prior *ab initio* calculations (Su et al., 2019a; Xu et al., 2020b), atomistic simulations (Xu et al., 2022), or experiments (Warlimont and Martienssen, 2018), and are summarized in Table 1. Given the low mismatch in a_0 between pure metals and alloys of the same lattice, the coherency strains are minute. In BCC and amorphous materials, there is no gradient energy in the system energy functional (Xu et al., 2020b). Hence, $\eta_{\alpha\beta}$ is non-zero only in the three FCC materials, i.e., Cu, $Cu_{0.9}Nb_{0.1}$, and $Cu_{0.8}Nb_{0.2}$. We remark that including the gradient energy into a PFDD model usually increases the calculation time by about 80%.

Here, a uniform coefficient (Xu et al., 2020a) is used, and so $\eta_{\alpha\beta}$ is simplified as η. In each FCC material, the following three steps are taken: (i) run eleven independent PFDD simulations with η varying from 0 to μb^2, in increment of $0.1\mu b^2$, to obtain eleven Shockley partial dislocation core sizes, (ii) run one atomistic simulation using the embedded-atom method interatomic potential (Zhang et al., 2013) to obtain one Shockley partial core size, and (iii) use linear interpolation to determine the value of η that allows PFDD to yield the same partial core size as atomistics. Similar procedures were taken to determine η in Ag (Xu et al., 2019c), Al (Xu et al., 2020a), Cu (Xu et al., 2019c), and Ni (Su et al., 2019b) in prior PFDD models, except that the ISF width instead of partial core size was used as a metric. A few recent works discussed the derivation and relevancy of the gradient energy term and its effects on dislocation core structures (Mianroodi et al., 2016; Xu et al., 2019b,c; Su et al., 2019b) and Peierls stresses (Xu et al., 2020a) in homogeneous FCC metals.

Table 2

Types of obstacles studied in seven cases of dislocation/obstacles interactions in a Cu matrix, as illustrated in Fig. 1. Phases of the three alloys can be found in Table 1.

Color	Case						
	A	B	C	D	E	F	G
Orange	Void	Void	Void	$Cu_{0.8}Nb_{0.2}$	$Cu_{0.8}Nb_{0.2}$	$Cu_{0.8}Nb_{0.2}$	$Cu_{0.5}Nb_{0.5}$
Cyan	Void	$Cu_{0.8}Nb_{0.2}$	$Cu_{0.5}Nb_{0.5}$	$Cu_{0.8}Nb_{0.2}$	$Cu_{0.9}Nb_{0.1}$	$Cu_{0.5}Nb_{0.5}$	$Cu_{0.5}Nb_{0.5}$

Table 3

Types of obstacles studied in six cases of dislocation/obstacles interactions in a Nb matrix, as illustrated in Fig. 1. Phases of the two alloys can be found in Table 1.

Color	Case					
	A	B	C	D	E	F
Orange	Void	$Cu_{0.1}Nb_{0.9}$	$Cu_{0.5}Nb_{0.5}$	$Cu_{0.5}Nb_{0.5}$	$Cu_{0.5}Nb_{0.5}$	$Cu_{0.1}Nb_{0.9}$
Cyan	Void	Void	Void	$Cu_{0.5}Nb_{0.5}$	$Cu_{0.1}Nb_{0.9}$	$Cu_{0.1}Nb_{0.9}$
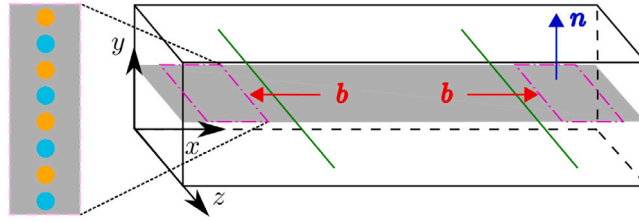
Fig. 1. Schematic of the simulation cell for an edge dislocation dipole interacting with two arrays of obstacles in a Cu or a Nb matrix. The gray parallelogram is the slip plane. Orange and cyan circles are obstacles which may or may not be of the same type. Specific obstacle types are summarized in Tables 2 and 3.

Using these parameters, we calculated the ISF width in Cu, $Cu_{0.9}Nb_{0.1}$, and $Cu_{0.8}Nb_{0.2}$, respectively, as 2.53 nm, 2.59 nm, and 2.63 nm. The Peierls stresses are $0.03355\mu_{Nb}$ (Xu et al., 2022) and $0.00035\mu_{Cu}$, respectively, in Nb and Cu. Note that the two values in Cu are respectively larger and lower than what were determined with η being zero: 2.31 nm and $0.00255\mu_{Cu}$ (Xu et al., 2022).

In heterogeneous materials, values of η in Table 1 for all materials but material 1 should be slightly modified before being used in Eq. (14) in its material 1-based dimensionless form, i.e.,

$$\eta^{[N]} = \eta \times \frac{\mu^{[N]}}{b^{[N]}b^{[N]}} \times \frac{b^{[1]}b^{[1]}}{\mu^{[1]}} \tag{16}$$

where $1 < N \le N_{\text{mat}}$.

2.3. Dislocation/obstacle interactions

As illustrated in Fig. 1, a dipole consisting of two edge dislocations with opposite Burgers vectors is built into a 3D periodic simulation cell. Let L_x, L_y, and L_z be the edge length of the cell along the x, y, and z direction, respectively. The two dislocations lie along the z axis on the mid-y plane, and are separated by $L_x/2$ along the x direction. The order parameters and their changes during the iterations are confined to the mid-y plane. Along the x, y, and z directions, respectively, 256, 64, and 128 grid points are employed. Two arrays of spherical obstacles are placed on the mid-y plane and are separated by $3L_x/4$ along the x direction. Each array contains eight obstacles, which can be voids, FCC $Cu_{0.9}Nb_{0.1}$, FCC $Cu_{0.8}Nb_{0.2}$, amorphous $Cu_{0.5}Nb_{0.5}$, or BCC $Cu_{0.1}Nb_{0.9}$. In each array, the obstacles are either of the same type or of the alternating type differentiated by the orange and cyan circles in Fig. 1. All cases studied in this paper are summarized in Tables 2 (Cu matrix) and 3 (Nb matrix).

We remark that the voids in this paper are "pseudo-voids" that were recently developed (Xu et al., 2022). Those voids are shearable by dislocations. The short-range dislocation/void interactions were captured via treating the void as a crystalline phase with a set of non-zero order parameters and exceedingly low moduli and GSFEs, i.e.,

$$C_{ijkl}^{\text{void}} = C_{ijkl}^{\text{matrix}}/N, \quad \gamma_{\text{gsf}}^{\text{void}} = \gamma_{\text{gsf}}^{\text{matrix}}/N \tag{17}$$

where $N = 10^5$ and 2×10^5 in a Cu and a Nb matrix, respectively. Note that the current work is the first one where a ψ_{gra}-included PFDD simulation is applied to a void-involved problem. For simplicity, we let $\eta^{\text{void}} = 0$.

2.4. Dislocation/interface interactions

Simulation cells for an edge dislocation dipole interacting with two 3D interfaces are illustrated in Fig. 2. They are similar to those for dislocation/obstacle interactions, except that (i) there are 1024 grid points along the x direction and (ii) two 3D interfaces
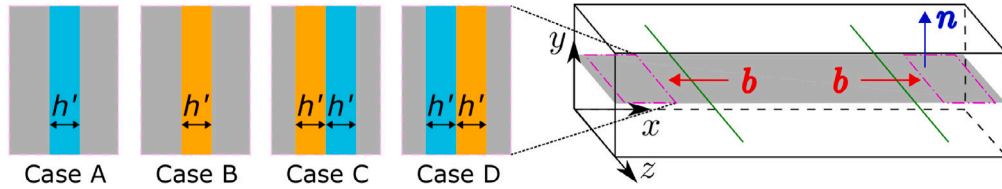
Fig. 2. Schematic of the simulation cell for an edge dislocation dipole interacting with two 3D interfaces in a Cu matrix. The gray parallelogram is the slip plane. Orange and cyan blocks denote FCC $Cu_{0.8}Nb_{0.2}$ and FCC $Cu_{0.9}Nb_{0.1}$, respectively.
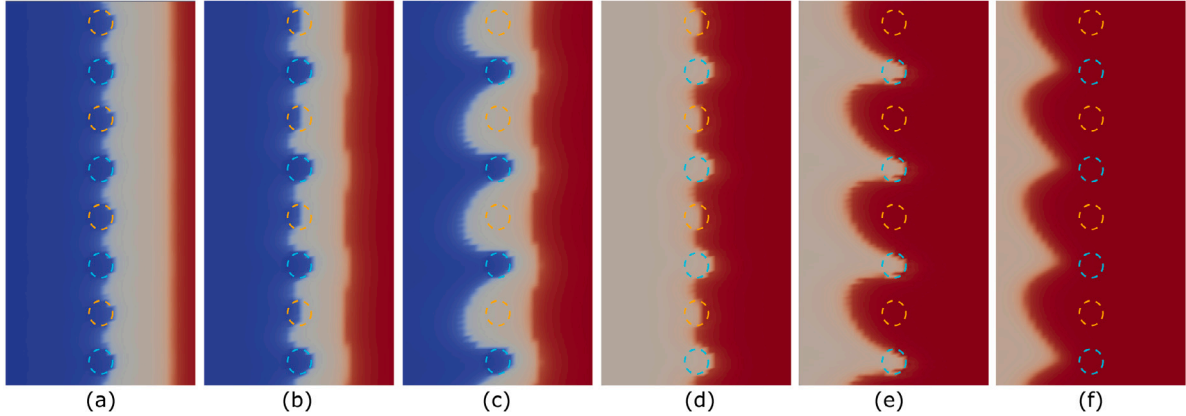

Fig. 3. Snapshots of selected configurations for an edge dislocation bypassing four FCC $Cu_{0.8}Nb_{0.2}$ precipitates (cyan circles) and four voids (orange circles) in a Cu matrix. The applied stress is constant and is slightly higher than the critical stress. Snapshots are colored by the disregistry field along the x direction, ξ_x, where blue and red correspond to $\xi_x = 0$ and b, respectively. The light brown region is the ISF between two Shockley partial dislocations.

separated by $7L_x/8$ along the x direction are introduced. Four types of 3D interfaces are studied, distinguished by the alloys and their arrangements. In cases A and B, the interface is monolayer and its thickness h' varies from 0.51 to 10.03 nm. In cases C and D, the interface is bilayer and its total thickness $2h'$ varies from 1.02 to 10.28 nm.

3. Results and discussion

3.1. Interactions between a dislocation and obstacles

In this section, we study interactions between an edge dislocation and eight obstacles. The obstacles are either of the same type or of alternating types (Fig. 1). Specific obstacle types are summarized in Table 2 when the matrix is Cu and in Table 3 when it is Nb.

3.1.1. Cu matrix

We first consider two exemplary cases in Cu. In the first case, all eight obstacles are shearable by dislocations while four of them are stronger barriers to dislocation glide than the other four. Examples include case B and case E in Table 2. In the second case, four of the eight obstacles are unshearable, while the remaining four are shearable. Examples are case C and case F in Table 2.

Fig. 3 presents snapshots at different moments as an edge dislocation bypasses an array of alternating FCC $Cu_{0.8}Nb_{0.2}$ precipitates and voids when the applied stress is slightly higher than the critical one. At first, portions of the leading partial dislocation extrude between adjacent obstacles, as shown in Fig. 3(a). Next, the leading partial transmits through the voids (Fig. 3(b)), followed by that the leading partial further extrudes between adjacent crystalline precipitates (Fig. 3(c)). Once the leading partial shears the crystalline precipitates and glides away, the trailing partial starts to extrude between adjacent obstacles (Fig. 3(d)), then shears the voids (Fig. 3(e)), and eventually shears the crystalline precipitates and glides away (Fig. 3(f)).

Fig. 4 is similar to Fig. 3, but for an edge dislocation bypassing an array of alternating FCC $Cu_{0.8}Nb_{0.2}$ precipitates and amorphous $Cu_{0.5}Nb_{0.5}$ precipitates. At first, the leading partial extrudes between adjacent precipitates because all eight of them pose non-negligible resistance to dislocation gliding (Fig. 4(a)). Then, since the amorphous precipitates are unshearable, the leading partial only cuts through the FCC precipitates while bowing around the amorphous ones before gliding away (Fig. 4(b,c)). The behavior of the trailing partial is very similar: extruding between all precipitates, shearing the FCC precipitates, bowing around the amorphous ones, and gliding away, as shown in Fig. 4(c–f).
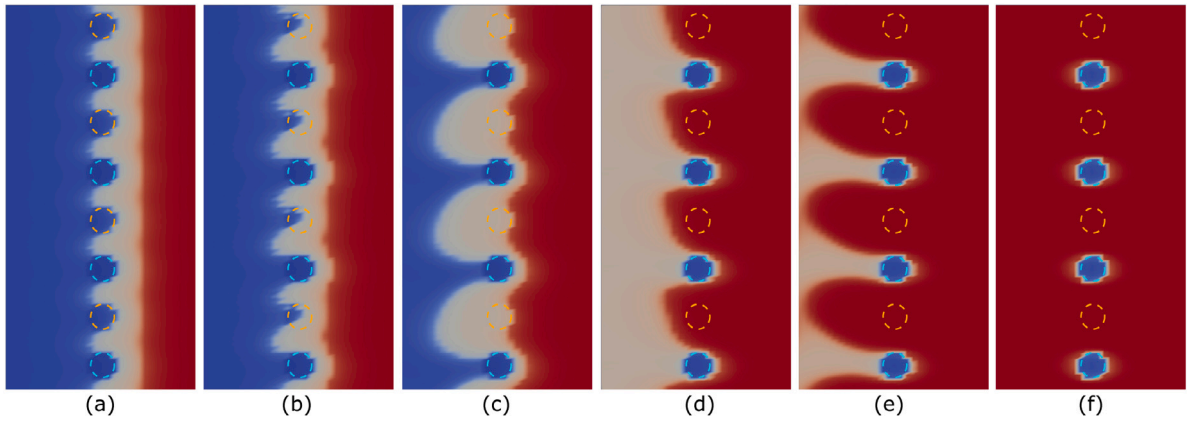
Fig. 4. Snapshots of selected configurations for an edge dislocation bypassing four FCC $Cu_{0.8}Nb_{0.2}$ precipitates (orange circles) and four amorphous $Cu_{0.5}Nb_{0.5}$ precipitates (cyan circles) in a Cu matrix. The applied stress is constant and is slightly higher than the critical stress. All snapshots are colored in the same way as Fig. 3.
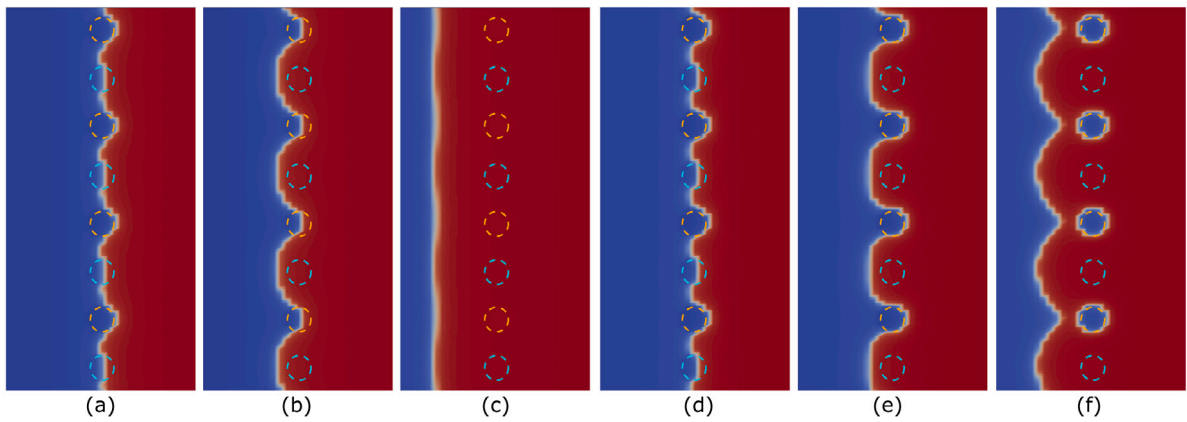

Fig. 5. Snapshots of selected configurations for an edge dislocation bypassing (a–c) four BCC $Cu_{0.1}Nb_{0.9}$ precipitates (orange circles) and four voids (cyan circles) or (d–f) four BCC $Cu_{0.1}Nb_{0.9}$ precipitates (cyan circles) and four amorphous $Cu_{0.5}Nb_{0.5}$ precipitates (orange circles) in a Nb matrix. The applied stress is constant and is slightly higher than the critical stress. All snapshots are colored in the same way as Fig. 3.

3.1.2. Nb matrix

Next, we turn our attention to dislocation/obstacle interactions in a Nb matrix. Similar to the Cu matrix, we focus on two representative cases, i.e., cases B and E in Table 3. In case B, four out of the eight obstacles are BCC $Cu_{0.1}Nb_{0.9}$ precipitates while the other four are voids. As shown in Fig. 5(a–c), the dislocation, which is undissociated, first shears the voids, then shears the BCC precipitates, and lastly glides away. In case E, four obstacles are also BCC $Cu_{0.1}Nb_{0.9}$ precipitates, but unlike in case B, the remaining four obstacles are now amorphous $Cu_{0.5}Nb_{0.5}$ precipitates. In this case, the dislocation only shears the BCC precipitates but not the amorphous ones. Eventually a shear loop is left behind around each amorphous precipitate, as shown in Fig. 5(d–f). Overall, the dislocation/obstacle interactions in a Nb matrix is similar to those in a Cu matrix, except that the entire dislocation moves together in Nb while two Shockley partial dislocations bypass the obstacle array sequentially in Cu.

Fig. 6 summarizes the critical stresses σ_c for an edge dislocation to bypass eight obstacles in a Cu or a Nb matrix. It is found that in the same matrix, σ_c for a dislocation to bypass alternating types of obstacles is between those for the same amount of uniform obstacles of each type. For example, in Cu, case C, in which there are four amorphous precipitates and four voids, corresponds to σ_c of about $0.0067\mu_{Cu}$. On the other hand, σ_c for eight amorphous precipitates and eight voids are about $0.021\mu_{Cu}$ and $0.0061\mu_{Cu}$, respectively. In other words, the critical stress for alternating precipitates and voids is closer to that for only voids. It is worth mentioning that this finding holds in all cases in both matrices, i.e., the critical stress for alternating obstacle type is always closer to that for the uniform obstacle of the weaker type, provided that both arrays contain the same amount of obstacles. This also suggests that simple linear interpolation between critical stress for stronger obstacles and that for weaker ones would not yield accurate critical stress for obstacles of alternating strength.
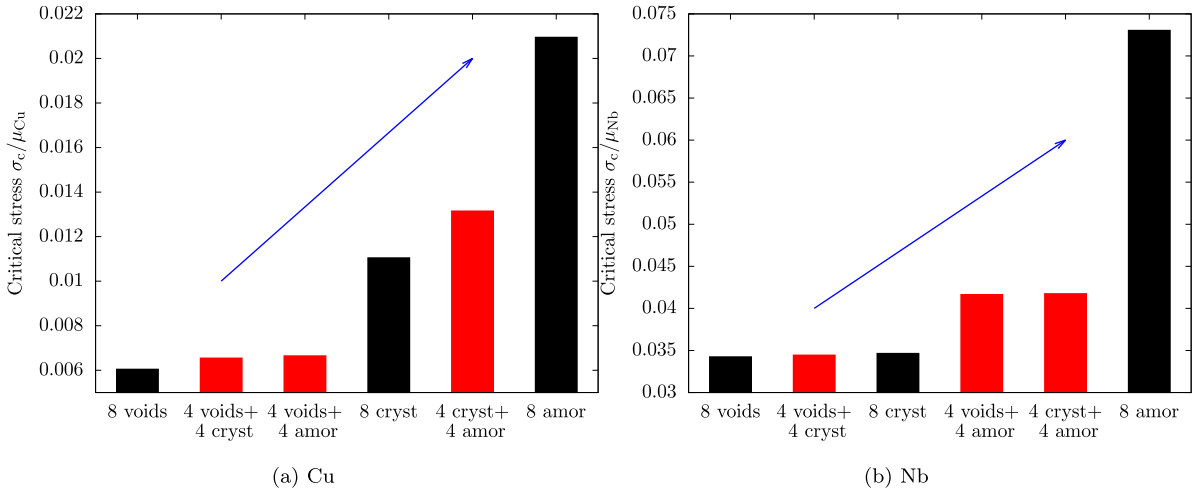
Fig. 6. Critical stresses for an edge dislocation to bypass eight obstacles in (a) Cu and (b) Nb. Black and red bars are based on uniform and alternating obstacle types, respectively. Note that in (a), the crystal is $Cu_{0.8}Nb_{0.2}$, not $Cu_{0.9}Nb_{0.1}$.
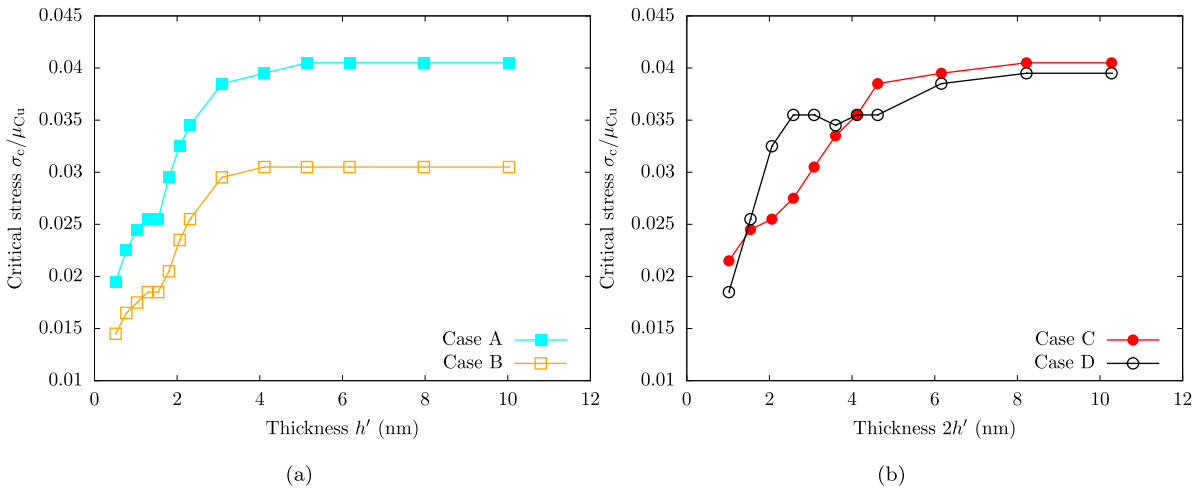

Fig. 7. Critical stresses for the transfer of an edge dislocation through a 3D interface in a Cu matrix, as a function of the interface thickness.

3.2. Slip transfer of a dislocation across a 3D interface

In this section, we study slip transfer of an edge dislocation across a 3D interface with a finite thickness in a Cu matrix. Four cases, summarized in Fig. 2, are studied. In each case, a series of interface thicknesses are considered.

The critical stresses for the edge dislocation to bypass the 3D interface are plotted as a function of the interface thickness in Fig. 7. We first focus on cases A and B. For the same interface thickness, the FCC $Cu_{0.9}Nb_{0.1}$ phase in case A is a stronger barrier to dislocation gliding than the FCC $Cu_{0.8}Nb_{0.2}$ phase in case B, in agreement with the results of dislocation/obstacle interactions. The critical stress generally increases with the interface thickness until 5.14 nm in case A or 4.11 nm in case B, above which the critical stress becomes a constant. In each case, there also exists a small stress plateau when the thickness is about 1.42 nm. To uncover the reason for the plateau, we study the position of the dissociated dislocation with respect to the 3D interface when the applied stress is slightly lower than the critical stress. At these sub-critical stresses, the dislocation does not bypass the entire interface. Instead, the trailing Shockley partial dislocation either is stuck within the 3D interface or has not reached the interface. Selected sub-critical configurations in cases A and B are shown in Fig. 8(a,b). With the narrowest 3D interface (0.51 nm), both partial dislocations are in the Cu matrix while the ISF spans over the interface. As the interface thickness increases, the sub-critical configurations in both cases become that the leading partial moves out of the interface while the trailing partial is still within.

Next, we turn our attention to cases C and D. The corresponding critical stresses are summarized in Fig. 7(b). In case C, the dislocation first encounters FCC $Cu_{0.9}Nb_{0.1}$, a harder phase, and then FCC $Cu_{0.8}Nb_{0.2}$, a weaker phase. In case D, it is the opposite. Selected sub-critical configurations for which the applied stress is slightly lower than the critical ones are shown in Fig. 8(c,d).
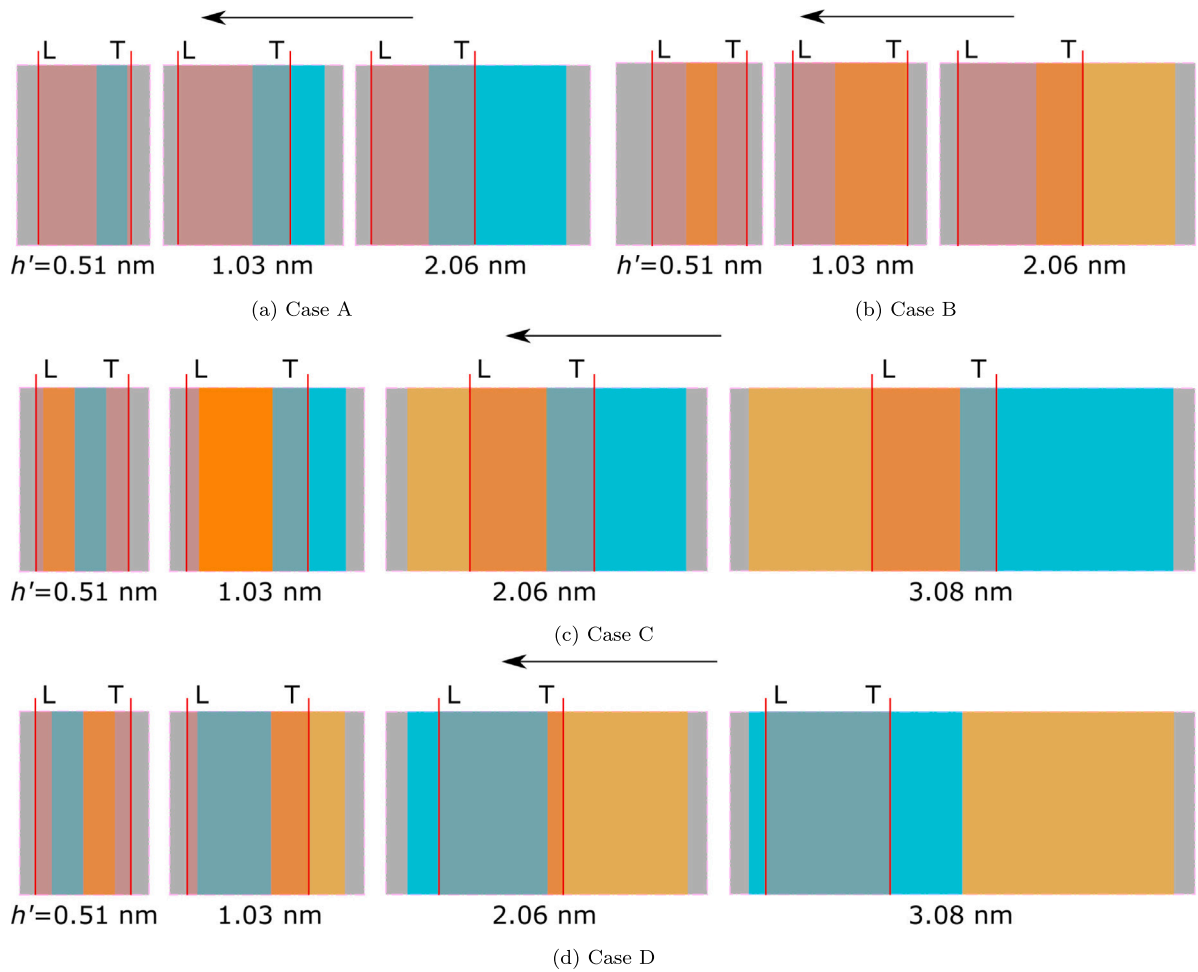
Fig. 8. Position of the dissociated dislocation near the 3D interface in cases A–D when the applied stress is slightly lower than the critical one. Two Shockley partial dislocations are denoted by two vertical red lines respectively, while the ISF by a semi-transparent red block between the two red lines. The leading and trailing partials are denoted by 'L' and 'T', respectively. In all cases, the dislocation moves from right to left, as indicated by the arrow.

Interestingly, for the same interface thickness, the critical stress in case C is higher than that in case D only when the 3D interface is either very thin (one phase being 0.51 nm) or sufficiently thick (one phase is ≥ 2.31 nm). Between cases A and B, the critical stresses in cases C and D are closer to case A than case B, suggesting that the critical stress for a dislocation to transmit through a heterogeneous 3D interface is mainly controlled by that through the stronger phase. Similar to cases A and B, the critical stresses in cases C and D converge to constants when one phase is thicker than 5.14 nm.

When the interface is thin, e.g., each phase is 0.51 nm thick, the ISF straddles the entire 3D interface containing two phases. As the interface thickness increases, the leading partial is still in the Cu matrix while the trailing partial is stuck in the phase that the dislocation encounters first. As the interface becomes thicker, two partials are stuck in different phases. The preceding statements hold for both cases C and D. With even thicker interfaces, the two partials are still in different phases in case C, but are both stuck in the latter phase, i.e., the stronger $Cu_{0.9}Nb_{0.1}$ phase, in case D. The change in the dislocation position in the sub-critical configuration in case D corresponds to the local stress minimum shown in Fig. 7(b). Note that the local stress minimum starts at an interface thickness $2h' = 2.58$ nm, which is close to the ISF width in Cu, 2.53 nm. On the other hand, there is no local stress minimum in case C, nor any stress plateau (which occurs in cases A and B).

4. Conclusions

In this work, we develop a PFDD model that takes into account multi-phase elastic heterogeneity, elastic anisotropy, and dissociated dislocations. Dislocations are able to glide in each phase as well as transmit across coherent boundaries between crystalline phases. The model is applied to two microstructures, distinct in the type and morphology. The first one is the in-plane interactions between an edge dislocation and an array of obstacles of either the same or alternating types. In a Cu matrix, four types of obstacles are considered: void, weak FCC phase, strong FCC phase, and amorphous phase. In a Nb matrix, three types of obstacles

are studied, including void, BCC phase, and amorphous phase. The newly developed PFDD model is found to successfully distinguish between different types of obstacles. For example, the dislocation first shears the weakest obstacles, i.e., voids, then a weaker crystalline phase, and lastly a stronger crystalline phase. The amorphous phases are, by design, unshearable by the dislocation, and so the dislocation line bows out around them, leaving behind shear loops. Both shearing and looping mechanisms were reported in prior atomistic simulations of dislocation/obstacle interactions (Xu et al., 2019a; Jian et al., 2020). Note that we did not study either unshearable crystalline precipitates (Adlakha et al., 2019) or shearable amorphous precipitates (Jian et al., 2022). For the former, PFDD can naturally reproduce the process of a dislocation bypassing a crystalline precipitate via the looping mechanism, e.g., when the precipitate has a sufficiently high GSFE. For the latter, the PFDD model needs to be further extended to consider the plastic deformation of amorphous materials, as discussed recently (Xu, 2022).

The second problem to which the multi-phase PFDD model is applied is the slip transfer of a dislocation across a 3D interface which contains either one or two crystalline phases. This study is motivated by recent experiments that a Cu/Nb system containing 3D interfaces possess simultaneously high strength and ductility (Chen et al., 2020; Cheng et al., 2022). Here, our PFDD simulations reveal that, regardless of the materials within the interface, the 3D interface is a stronger barrier to dislocation gliding than a 2D one. However, the interface strength does not increase indefinitely with its thickness but converges to a constant when it is sufficiently thick. When the interface thickness is close to the ISF width of the dislocation, there exists a local stress minimum in one of the four cases studied here.

In either problem, we find that when the dislocation barrier itself is heterogeneous, its resistance to dislocation gliding cannot be predicted by linearly interpolated from the resistances of individual phases. In dislocation/obstacle interactions, the critical stress is mainly determined by the weaker obstacles, while in dislocation/interface interactions, the critical stress is chiefly controlled by the stronger phases. Future work may consider four or more phases in the simulation or the coexistence of BCC and FCC crystalline phases.

CRediT authorship contribution statement

Shuozhi Xu: Conceptualization, Methodology, Software, Formal analysis, Visualization, Writing – original draft, Writing – review & editing. **Justin Y. Cheng:** Data curation, Investigation, Writing – review & editing. **Nathan A. Mara:** Supervision, Funding acquisition, Writing – review & editing. **Irene J. Beyerlein:** Conceptualization, Supervision, Funding acquisition, Writing – review & editing.

Declaration of competing interest

The authors declare that they have no known competing financial interests or personal relationships that could have appeared to influence the work reported in this paper.

Data availability

Data will be made available on request.

Acknowledgments

References

Adlakha, I., Garg, P., Solanki, K.N., 2019. Revealing the atomistic nature of dislocation-precipitate interactions in Al-Cu alloys. J. Alloys Compd. 797, 325–333. http://dx.doi.org/10.1016/j.jallcom.2019.05.110.

Alexandrov, D.V., Zubarev, A.Y., 2019. Heterogeneous materials: metastable and non-ergodic internal structures. Philos. Trans. R. Soc. Lond. Ser. A Math. Phys. Eng. Sci. 377 (2143), 20180353. http://dx.doi.org/10.1098/rsta.2018.0353.

Bertin, N., Sills, R.B., Cai, W., 2020. Frontiers in the simulation of dislocations. Annu. Rev. Mater. Res. 50 (1), 437–464. http://dx.doi.org/10.1146/annurev-matsci-091819-015500.

Beyerlein, I.J., Xu, S., Llorca, J., El-Awady, J.A., Mianroodi, J.R., Svendsen, B., 2019. Alloy design for mechanical properties: Conquering the length scales. MRS Bull. 44 (4), 257–265. http://dx.doi.org/10.1557/mrs.2019.67.

Chen, Y., Li, N., Hoagland, R.G., Liu, X.Y., Baldwin, J.K., Beyerlein, I.J., Cheng, J.Y., Mara, N.A., 2020. Effects of three-dimensional Cu/Nb interfaces on strengthening and shear banding in nanoscale metallic multilayers. Acta Mater. 199, 593–601. http://dx.doi.org/10.1016/j.actamat.2020.08.019.

Cheng, J.Y., Xu, S., Chen, Y., Li, Z., Baldwin, J.K., Beyerlein, I.J., Mara, N.A., 2022. Simultaneous high-strength and deformable nanolaminates with thick biphase interfaces. Nano Lett. 22 (5), 1897–1904. http://dx.doi.org/10.1021/acs.nanolett.1c04144.

Eshelby, J.D., 1957. The determination of the elastic field of an ellipsoidal inclusion, and related problems. Proc. R. Soc. Lond. Ser. A Math. Phys. Eng. Sci. 241 (1226), 376–396. http://dx.doi.org/10.1098/rspa.1957.0133.

Jian, W.-R., Xu, S., Su, Y., Beyerlein, I.J., 2022. Energetically favorable dislocation/nanobubble bypass mechanism in irradiation conditions. Acta Mater. 230, 117849. http://dx.doi.org/10.1016/j.actamat.2022.117849.

Jian, W.-R., Zhang, M., Xu, S., Beyerlein, I.J., 2020. Atomistic simulations of dynamics of an edge dislocation and its interaction with a void in copper: a comparative study. Model. Simul. Mater. Sci. Eng. 28 (4), 045004. http://dx.doi.org/10.1088/1361-651X/ab8358.

Lu, L., Wu, X., Beyerlein, I.J., 2020. Preface to the viewpoint set on: Heterogeneous gradient and laminated materials. Scr. Mater. 187, 307–308. http://dx.doi.org/10.1016/j.scriptamat.2020.06.036.

Mianroodi, J.R., Hunter, A., Beyerlein, I., Svendsen, B., 2016. Theoretical and computational comparison of models for dislocation dissociation and stacking fault / core formation in fcc crystals. J. Mech. Phys. Solids 95, 719–741. http://dx.doi.org/10.1016/j.jmps.2016.04.029.

Mianroodi, J.R., Shanthraj, P., Kontis, P., Cormier, J., Gault, B., Svendsen, B., Raabe, D., 2019. Atomistic phase field chemomechanical modeling of dislocation-solute-precipitate interaction in Ni-Al-Co. Acta Mater. 175, 250–261. http://dx.doi.org/10.1016/j.actamat.2019.06.008.

Noell, P.J., Sabisch, J.E.C., Medlin, D.L., Boyce, B.L., 2020. Nanoscale conditions for ductile void nucleation in copper: Vacancy condensation and the growth-limited microstructural state. Acta Mater. 184, 211–224. http://dx.doi.org/10.1016/j.actamat.2019.11.022.

Peng, S., Wei, Y., Gao, H., 2020. Nanoscale precipitates as sustainable dislocation sources for enhanced ductility and high strength. Proc. Natl. Acad. Sci. USA 117 (10), 5204–5209. http://dx.doi.org/10.1073/pnas.1914615117.

Po, G., Mohamed, M.S., Crosby, T., Erel, C., El-Azab, A., Ghoniem, N., 2014. Recent progress in discrete dislocation dynamics and its applications to micro plasticity. JOM 66 (10), 2108–2120. http://dx.doi.org/10.1007/s11837-014-1153-2.

Quek, S.S., Wu, Z., Zhang, Y.W., Srolovitz, D.J., 2014. Polycrystal deformation in a discrete dislocation dynamics framework. Acta Mater. 75, 92–105. http://dx.doi.org/10.1016/j.actamat.2014.04.063.

Su, Y., Xu, S., Beyerlein, I.J., 2019a. Density functional theory calculations of generalized stacking fault energy surfaces for eight face-centered cubic transition metals. J. Appl. Phys. 126 (10), 105112. http://dx.doi.org/10.1063/1.5115282.

Su, Y., Xu, S., Beyerlein, I.J., 2019b. *Ab initio*-informed phase-field modeling of dislocation core structures in equal-molar coniru multi-principal element alloys. Model. Simul. Mater. Sci. Eng. 27 (8), 084001. http://dx.doi.org/10.1088/1361-651X/ab3b62.

Wang, Y.U., Jin, Y.M., Cuitiño, A.M., Khachaturyan, A.G., 2001. Nanoscale phase field microelasticity theory of dislocations: model and 3D simulations. Acta Mater. 49 (10), 1847–1857. http://dx.doi.org/10.1016/S1359-6454(01)00075-1.

Wang, Y.U., Jin, Y.M., Khachaturyan, A.G., 2003. Phase field microelasticity modeling of dislocation dynamics near free surface and in heteroepitaxial thin films. Acta Mater. 51 (14), 4209–4223. http://dx.doi.org/10.1016/S1359-6454(03)00238-6.

Wang, Y., Li, J., 2010. Phase field modeling of defects and deformation. Acta Mater. 58 (4), 1212–1235. http://dx.doi.org/10.1016/j.actamat.2009.10.041.

Warlimont, H., Martienssen, W. (Eds.), 2018. Springer Handbook of Materials Data, second ed. In: Springer Handbooks, Springer International Publishing, http://dx.doi.org/10.1007/978-3-319-69743-7.

Wu, K., Liu, G., Yu, P., Ye, C., Shi, J., Shen, Y., 2022. Prediction of hardening effect by irradiation-induced vacancy clusters with dislocation dynamics. Int. J. Plast. 149, 103160. http://dx.doi.org/10.1016/j.ijplas.2021.103160.

Wu, X., Yang, M., Yuan, F., Wu, G., Wei, Y., Huang, X., Zhu, Y., 2015. Heterogeneous lamella structure unites ultrafine-grain strength with coarse-grain ductility. Proc. Natl. Acad. Sci. USA 112 (47), 14501–14505. http://dx.doi.org/10.1073/pnas.1517193112.

Wu, X., Zhu, Y., 2017. Heterogeneous materials: a new class of materials with unprecedented mechanical properties. Mater. Res. Lett. 5 (8), 527–532. http://dx.doi.org/10.1080/21663831.2017.1343208.

Xu, S., 2022. Recent progress in the phase-field dislocation dynamics method. Comput. Mater. Sci. 210, 111419. http://dx.doi.org/10.1016/j.commatsci.2022.111419.

Xu, S., Cheng, J.Y., Li, Z., Mara, N.A., Beyerlein, I.J., 2022. Phase-field modeling of the interactions between an edge dislocation and an array of obstacles. Comput. Methods Appl. Mech. Engrg. 389, 114426. http://dx.doi.org/10.1016/j.cma.2021.114426.

Xu, S., McDowell, D.L., Beyerlein, I.J., 2019a. Sequential obstacle interactions with dislocations in a planar array. Acta Mater. 174, 160–172. http://dx.doi.org/10.1016/j.actamat.2019.05.030.

Xu, S., Mianroodi, J.R., Hunter, A., Svendsen, B., Beyerlein, I.J., 2020a. Comparative modeling of the disregistry and Peierls stress for dissociated edge and screw dislocations in Al. Int. J. Plast. 129, 102689. http://dx.doi.org/10.1016/j.ijplas.2020.102689.

Xu, S., Smith, L., Mianroodi, J.R., Hunter, A., Svendsen, B., Beyerlein, I.J., 2019b. A comparison of different continuum approaches in modeling mixed-type dislocations in Al. Model. Simul. Mater. Sci. Eng. 27 (7), 074004. http://dx.doi.org/10.1088/1361-651X/ab2d16.

Xu, S., Su, Y., Beyerlein, I.J., 2019c. Modeling dislocations with arbitrary character angle in face-centered cubic transition metals using the phase-field dislocation dynamics method with full anisotropic elasticity. Mech. Mater. 139, 103200. http://dx.doi.org/10.1016/j.mechmat.2019.103200.

Xu, S., Su, Y., Smith, L.T.W., Beyerlein, I.J., 2020b. Frank-read source operation in six body-centered cubic refractory metals. J. Mech. Phys. Solids 141, 104017. http://dx.doi.org/10.1016/j.jmps.2020.104017.

Zeng, Y., Hunter, A., Beyerlein, I.J., Koslowski, M., 2016. A phase field dislocation dynamics model for a bicrystal interface system: An investigation into dislocation slip transmission across cube-on-cube interfaces. Int. J. Plast. 79, 293–313. http://dx.doi.org/10.1016/j.ijplas.2015.09.001.

Zhang, L., Martinez, E., Caro, A., Liu, X.-Y., Demkowicz, M.J., 2013. Liquid-phase thermodynamics and structures in the Cu-Nb binary system. Model. Simul. Mater. Sci. Eng. 21 (2), 025005. http://dx.doi.org/10.1088/0965-0393/21/2/025005.

Zheng, S., Beyerlein, I.J., Carpenter, J.S., Kang, K., Wang, J., Han, W., Mara, N.A., 2013. High-strength and thermally stable bulk nanolayered composites due to twin-induced interfaces. Nat. Comm. 4 (1), 1696. http://dx.doi.org/10.1038/ncomms2651.

Zhu, Y., Ameyama, K., Anderson, P.M., Beyerlein, I.J., Gao, H., Kim, H.S., Lavernia, E., Mathaudhu, S., Mughrabi, H., Ritchie, R.O., Tsuji, N., Zhang, X., Wu, X., 2021. Heterostructured materials: superior properties from hetero-zone interaction. Mater. Res. Lett. 9 (1), 1–31. http://dx.doi.org/10.1080/21663831.2020.1796836.